



# Inter-decadal variability of the heat source over the Tibetan Plateau

Jingchen Liu<sup>1,3</sup> · Xiaodan Guan<sup>1,2</sup> · Zhaokui Gao<sup>1</sup> · Xiaoqian Huang<sup>1</sup> · Jieru Ma<sup>1</sup> · Yongli He<sup>1</sup> · Tiejun Xie<sup>4</sup>

Received: 10 January 2021 / Accepted: 9 August 2021

© The Author(s), under exclusive licence to Springer-Verlag GmbH Germany, part of Springer Nature 2021

## Abstract

The vertically integrated apparent heat source ( $\langle Q_1 \rangle$ ), reflecting features and evolutions of the heat budget, is a key variable in the changing climate of the Tibetan Plateau (TP). Despite previous investigations, characteristics of  $\langle Q_1 \rangle$  on the inter-decadal timescale have not received sufficient attention. By extracting the inter-decadal variability (IDV) using the ensemble empirical mode decomposition (EEMD) method, results from our analysis reveal the dominant role of IDV of  $\langle Q_1 \rangle$  over the TP.  $\langle Q_1 \rangle$  variability is closely related to the Indian Ocean sea surface temperature (IOSST) and Pacific Decadal Oscillation (PDO) at the inter-decadal timescale. During the IOSST and PDO in-phase combinations (i.e., positive IOSST with positive PDO phase and negative IOSST with negative PDO phase), a low pressure (high pressure) system occurred over the TP which was accompanied by cyclonic (anticyclonic) circulation bringing cold (warm) air from the North Pacific (Indian Ocean), resulting in an obvious net loss (gain) of heat over the central and northeastern TP. In the future, IDV will still dominate the change of  $\langle Q_1 \rangle$  over the TP, having a shortened cycle and reduced amplitude under a scenario of intensified emissions.

**Keywords** Tibetan Plateau · Inter-decadal variability · Indian Ocean sea surface temperature · Pacific Decadal Oscillation · CMIP6

## 1 Introduction

The Tibetan Plateau (TP) is located in the subtropical eastern-central Eurasian continent. It has the highest average altitude and the most complex topography in the world. Its mechanical and thermal-dynamical effects have significant impacts on atmospheric circulation and climate within the Asian region and across the world (e.g., Wu et al. 2007; Zhou et al. 2009; Duan et al. 2012). The heat budget over the TP is especially important for its roles in global climate variability. For example, the strong thermal forcing of the TP has a profound impact on atmospheric circulation (Wang et al.

2018), modulating the evolution, intensity and rainfall patterns of the Asian summer monsoon (Wu and Zhang 1998; Wu et al. 2007). The East Asian monsoon and the eastern part of the South Asian monsoon are controlled by thermal forcing of the TP (Wu et al. 2012). The direct thermal effect of the Tibetan–Iranian Plateau produces a lower troposphere cyclonic circulation in the surrounding area, increasing continental precipitation over South and East Asia (He et al. 2019).

Since the beginning of the 1980s, the TP has experienced climate variations which have affected atmospheric and hydrological cycles (Yang et al. 2014; Wu et al. 2020). As unusual warming over the TP is accompanied by a change in atmospheric heat sources, more attention has been paid to factors which control the variability of atmospheric heat sources over the TP. It has been shown that weakened sensible heat flux (SH) in spring and summer, as well as enhanced radiative convergence in summer and autumn, leads to a decline in annual-mean atmospheric heat source over the western TP (Duan and Wu 2008). Oceanic modes as the external factors can modify atmospheric circulation between the TP and oceanic regions and affecting atmospheric vertical and horizontal motions over the TP, thus inducing local dynamically-induced temperature warming

✉ Xiaodan Guan  
guanxd@lzu.edu.cn

<sup>1</sup> Key Laboratory for Semi-Arid Climate Change of the Ministry of Education, College of Atmospheric Sciences, Lanzhou University, Lanzhou 730000, China

<sup>2</sup> Collaborative Innovation Center for Western Ecological Safety, Lanzhou 730000, China

<sup>3</sup> Jiashan County Meteorological Bureau, Jiashan 314100, China

<sup>4</sup> College of Global Change and Earth System Sciences (GCESS), Beijing Normal University, Beijing 100875, China

and climate change over the whole TP (Ma et al. 2017). The Indian Ocean sea surface temperature (IOSST) anomaly can alter the thermal forcing of the TP on an inter-annual timescale (Zhao et al. 2018). Jin et al. (2016) proposed that the TP heat source could be influenced by the decaying El Niño–Southern Oscillation (ENSO) and wave train triggered by the IOSST anomaly. The Pacific Decadal Oscillation (PDO) is the most dominant mode of the inter-decadal sea surface temperature (SST) oscillation in the North Pacific (Mantua et al. 1997; Zhang et al. 1997). In recent decades, the portion of SH variation over the TP related to the change in surface wind speed is mainly attributed to the dynamic process related to the PDO (Zhu et al. 2018). When the PDO enters its warm phase, warm and wet conditions are transported to the East Asian continent through the southerly wind anomalies along the western flank of the anomalous high pressure (Kim et al. 2014) which can further influence the heat budget over the TP. In addition, the PDO has an effect on the inter-decadal characteristics of the Indian Ocean Dipole (Krishnamurthy and Krishnamurthy 2016), and multi-decadal variability of the Pacific SST has a great driving effect on the IOSST (Dong et al. 2016). Until recently, investigations examining inter-decadal variability (IDV) of the vertically integrated apparent heat source ( $\langle Q_1 \rangle$ ) over the TP and its potential connection with the combined effect of the IOSST and PDO at the inter-decadal timescale have remained unclear.

As the  $\langle Q_1 \rangle$  is conducive to understanding the heat budget over the TP, the main objectives of this study were to quantify the IDV of the  $\langle Q_1 \rangle$  over the TP and identify its possible connection with the IOSST and PDO. Details of methodology and data are described in Sect. 2. In Sect. 3, we analyze the inter-decadal behaviors of  $\langle Q_1 \rangle$  over the TP. We also explore the relationships of IOSST and PDO with  $\langle Q_1 \rangle$ , and compare the corresponding features simulated by the Coupled Model Intercomparison Project Phase 6 (CMIP6) models. Finally, conclusions and discussion are presented in Sect. 4.

## 2 Data and methods

### 2.1 Data sources

The main data used in this study derived from the Japanese 55-year Reanalysis (JRA-55) produced by the Japan Meteorological Agency (JMA; Kobayashi et al. 2015) for the period 1958–2017, having a horizontal resolution of  $1.25^\circ \times 1.25^\circ$ . JRA-55 reanalysis data have been shown to have a good performance over the TP (Chen et al. 2014). Reanalysis data products have been used in previous investigations to examine changes in heat source (Li et al. 2017) and total column of water vapor over the TP (Wang et al. 2019). In addition,

observations of meteorological variables (i.e., air temperature, vertical velocity, wind velocity and surface pressure) have also been used to analyze  $\langle Q_1 \rangle$ .

For SST observational data, HadISST (V1.1; Rayner et al. 2003) data was downloaded from the Met Office Hadley Centre, having a horizontal resolution of  $1^\circ \times 1^\circ$ . Annual IOSST is defined as the area-weighted mean SST of the Indian Ocean region ( $20^\circ \text{S}$ – $10^\circ \text{N}$ ,  $60^\circ$ – $100^\circ \text{E}$ ) (Xie et al. 2021). The PDO index was derived from the Joint Institute for the Study of the Atmosphere and Ocean (JISAO). This index was defined as the leading Empirical Orthogonal Function (EOF) of the mean November–March de-trended SST anomalies for the Pacific Ocean to the north of  $20^\circ \text{N}$  (Parker et al. 1995; Reynolds et al. 2002). The ENSO index is obtained from the the Japan Meteorological Agency (JMA). This index is widely used for studying ENSO events (e.g., Birk et al. 2010; Kim et al. 2014). The ENSO index used is a 5-month running mean of spatially averaged SST anomalies over the eastern tropical Pacific ( $4^\circ \text{S}$ – $4^\circ \text{N}$ ,  $150^\circ$ – $90^\circ \text{W}$ ). And the Atlantic Multidecadal Oscillation (AMO) index is obtained from the Earth System Research Laboratory (ESRL). For all datasets, the period spanning 1958–2017 was analyzed.

In our analysis we used outputs of 13 models (Table 1) from Coupled Model Intercomparison Project Phase 6 (CMIP6). We applied the historical simulations from 1850 to 2014 and future climate projections (O'Neill et al. 2016) until 2100 under the two Shared Socioeconomic Pathways (SSPs) of SSP245 and SSP585 with medium and high radiative forcing, respectively (Meehl et al. 2014; O'Neill et al. 2014; van Vuuren et al. 2014). To compare the historical simulations of model outputs with JRA-55 data, we interpolate different horizontal resolutions of simulated variables consistently into JRA-55 resolution using bilinear interpolation.

### 2.2 Diagnostic methods

Following previous investigations (Yanai et al. 1973; Yanai and Tomita 1998), the apparent heat source  $Q_1$  can be calculated using:

$$Q_1 = c_p \left( \frac{p}{p_0} \right)^\kappa \left( \frac{\partial \theta}{\partial t} + V \cdot \nabla \theta + \omega \frac{\partial \theta}{\partial p} \right), \quad (1)$$

where  $\theta$  is the potential temperature (units: K);  $V$  is the horizontal wind (units: m/s);  $\omega$  is the vertical velocity on isobaric surface (units: Pa/s);  $p$  is the pressure (units: Pa);  $p_0 = 1000 \text{ hPa}$  and  $\kappa = \frac{R}{c_p}$  (units: J/(kg K)).  $R$  and  $c_p$  are the gas constant and specific heat at constant pressure of dry air, respectively; and  $\nabla$  is the isobaric gradient operator.

The vertically integrated apparent heat source ( $\langle Q_1 \rangle$ ) was obtained by integrating Eq. (1), where  $p_s$  is the surface

**Table 1** Summary of CMIP6 models used in this study

Model name	Resolutions	Modeling center	Data references
BCC-CSM2-MR	160×320	Beijing Climate Center, China	Xin et al. (2019)
CanESM5	64×128	Canadian Centre for Climate Modeling and Analysis, Canada	Swart et al. (2019)
CESM2	192×288	National Center for Atmospheric Research, United States	Danabasoglu 2019
CESM2-WACCM	192×288	National Center for Atmospheric Research, United States	Danabasoglu (2019)
FGOALS-f3-L	180×360	Chinese Academy of Sciences, China	Yu (2019)
GFDL-ESM4	180×360	NOAA Geophysical Fluid Dynamics Laboratory, United States	John et al. (2018)
INM-CM4-8	120×180	Institute of Numerical Mathematics, Russia	Volodin et al. (2019a)
INM-CM5-0	120×180	Institute of Numerical Mathematics, Russia	Volodin et al. 2019b
MIROC6	128×256	Atmosphere and Ocean Research Institute, Japan	Shiogama et al. (2019)
MPI-ESM1-2-HR	192×384	Max Planck Institute for Meteorology, Germany	Schupfner et al. (2019)
MPI-ESM1-2-LR	96×192	Max Planck Institute for Meteorology, Germany	Wieners et al. (2019)
MRI-ESM2-0	160×320	Meteorological Research Institute, Japan	Yukimoto et al. (2019)
NESM3	96×192	Nanjing University of Information Science and Technology, China	Cao (2019)

pressure level. As the average elevation of the TP is approximately 4000 m, the minimum of  $p_s$  used in this study is 600 hPa, as:

$$Q_1 = \frac{1}{g} \int_{100}^{p_s} Q_1 dp, \quad (2)$$

Note that positive (negative)  $\langle Q_1 \rangle$  indicates a net heat gain (loss).

### 2.3 Ensemble empirical mode decomposition method

In this study, the ensemble empirical mode decomposition (EEMD) method was adopted in this study to decompose the time series of  $\langle Q_1 \rangle$ . This method is an adaptive and noise-assisted data analysis method; suitable for non-stationary and nonlinear signal detection, developed from the popular empirical mode decomposition (EMD) (Huang et al. 1998). Original climate signals can be decomposed into different oscillatory components with different time scales (intrinsic mode function [IMF]) and trends. As per the methods of Ji et al. (2014), the steps in the EEMD method are:

(1) Add a white noise series to the targeted data series  $y(t)$ .

(2.1) Set  $y_1(t) = y(t)$  and identify all the maxima and minima values of  $y_1(t)$ , connect all maxima points to obtain the upper envelope  $e_u(t)$  and connect all minima points to obtain the lower envelope  $e_l(t)$  with cubic splines, respectively.

(2.2) According to the given criteria, calculate the mean  $m(t)$  between the two envelopes as,

$$m(t) = [e_u(t) + e_l(t)]/2 \quad (3)$$

It is important to determine whether  $m(t)$  is close to zero (equivalent to the symmetric of the upper and lower envelopes about the zero line) at any location.

(2.3) If  $m(t)$  is close to zero, stop the screening process. Otherwise, set  $y_1(t) = y(t) - m(t)$  and repeat steps 2.1 and 2.2.

(2.4) Subsequently, the original time series  $y(t)$  can be expressed as the first intrinsic mode function (IMF) and a remainder. If the remainder still contains oscillatory components, repeat steps 2.1 and 2.2 and set  $y_1(t)$  as the remainder.

As each time series can be decomposed into different IMFs and a remainder, it can be expressed as:

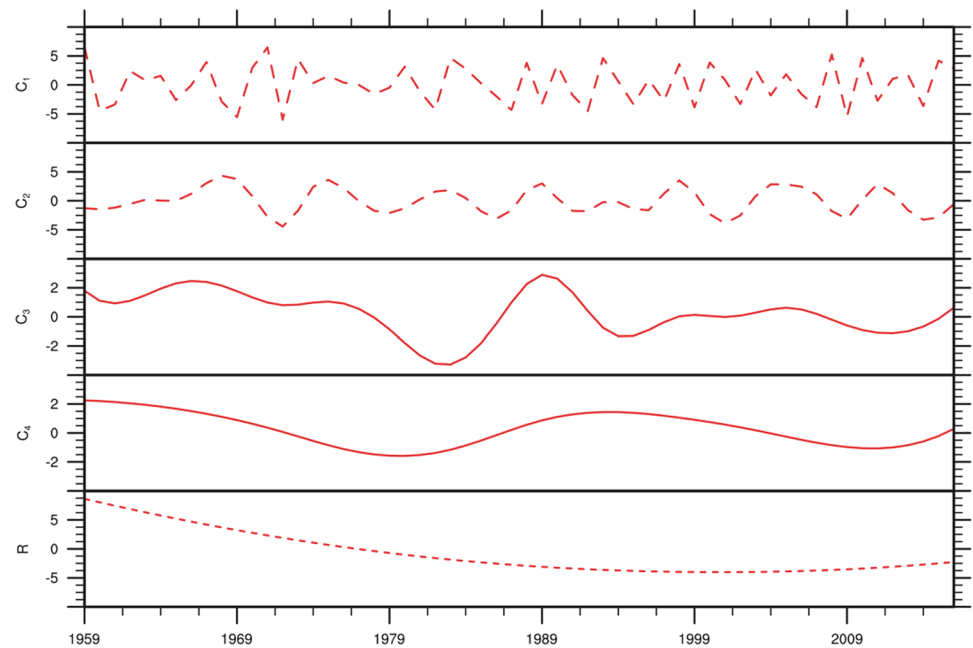
$$y(t) = \sum_{j=1}^n C_j(t) + R_n(t) \quad (4)$$

where  $n$  indicates the number of IMFs;  $C_j(t)$  indicates the  $j$ th IMF; and  $R_n(t)$  denotes the final remainder which is either monotonic or contains only one extreme.

(3) Steps 1 and 2 are repeated again with different white noise series being added each time to obtain (ensemble) mean values for corresponding IMFs of the decompositions as the final result.

According to Ji et al. (2014), noise added to the data has an amplitude that is 0.2 times the standard deviation of the raw data, and the ensemble number is 400. The number of IMFs is 5. As the EEMD method can split the evolution of climate variability into long-term trends and oscillation components (Wu et al. 2011; Ji et al. 2014), we applied the EEMD method to decompose the time series of  $\langle Q_1 \rangle$  anomalies over the TP to obtain four IMF components ( $C_{1-4}$ ) and a remainder (Fig. 1). The IMFs are a set of components at different timescales and the remainder is the intrinsic nonlinear secular trend (R). Due to the IMFs  $C_3$  and  $C_4$  are at the inter-decadal timescale, and their sum

**Fig. 1** EEMD decomposition of the time series of annual  $\langle Q_1 \rangle$  anomaly over the TP



is named as the inter-decadal variability (IDV). IMFs  $C_1$  and  $C_2$  are at the inter-annual timescale and their sum is called the inter-annual variability (IAV) (Wei et al. 2019).

Regarding the EEMD method, the error related to the data end effect is tied to the determination of values of envelopes at the data ends in every recurrence of the sifting process (Wu et al. 2011). Therefore, the first and last years of all decomposed results were excluded to eliminate minor influences of the end effect on our results (Qian et al. 2011). JRA-55 data spanning 1958–2017 was used in this study, leaving the period of 1959–2016 after EEMD decomposition for further analysis. CMIP6 historical simulations and future climate projections used in this study cover the periods 1958–2014 and 2015–2100, respectively; also leaving the periods 1959–2013 and 2016–2099 after EEMD decomposition for comparison and future prediction, respectively.

IDVs of both annual IOSST and PDO were extracted by applying the EEMD method. Positive (negative) phase corresponds to the IDVs above (below) zero. There were 34 positive IOSST (red bars in Fig. 2) and 24 negative IOSST (blue bars in Fig. 2) years, along with 28 positive and 30 negative PDO years. For convenience, positive (negative) IOSST phases are denoted as +IOSST (-IOSST). +IOSST combined with a positive (negative) phase of the PDO will be referred to as +IOSST/+PDO (+IOSST/-PDO). Similarly, -IOSST combined with a positive (negative) phase of PDO will be termed as -IOSST/+PDO (-IOSST/-PDO). The classification of years associated with the phases of IOSST and PDO are displayed in Table 2; annual IOSST and PDO indices are presented in Fig. 2.

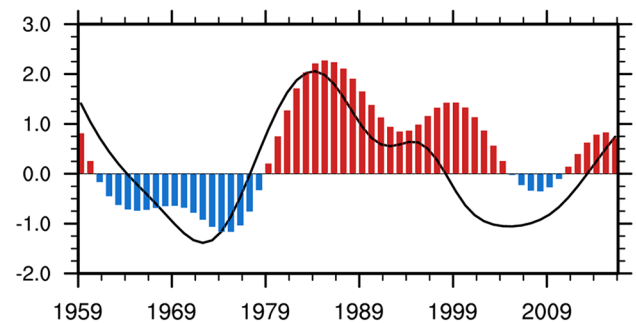


**Fig. 2** The IDV of annual IOSST (bars) and PDO index (black curve) during 1959–2016. Red and blue bars indicate the positive and negative IOSST years, respectively

**Table 2** Classification of years based on the phases of IOSST and PDO on the inter-decadal scale for the period of 1959–2016

	Positive PDO	Negative PDO
Positive IOSST	1959–1960, 1979–1997, 2014–2016	1998–2004, 2011–2013
Negative IOSST	1961–1963, 1978	1964–1977, 2005–2010

### 3 Results

#### 3.1 Inter-decadal variability of $\langle Q_1 \rangle$ over the TP

$\langle Q_1 \rangle$  time series of (red curve) anomaly results over the TP during 1958–2017 (Fig. 3) indicate that annual temporal variations recorded a fluctuating downward trend

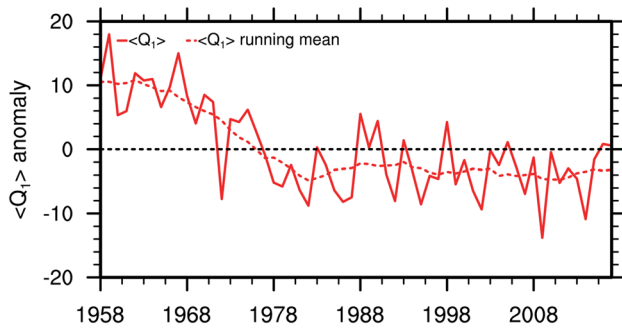


**Fig. 3** The time series of annual  $\langle Q_1 \rangle$  anomalies (units:  $\text{W/m}^2$ ) over the TP. Solid curves represent the time series of the original data, and dashed ones are the 11-year running means

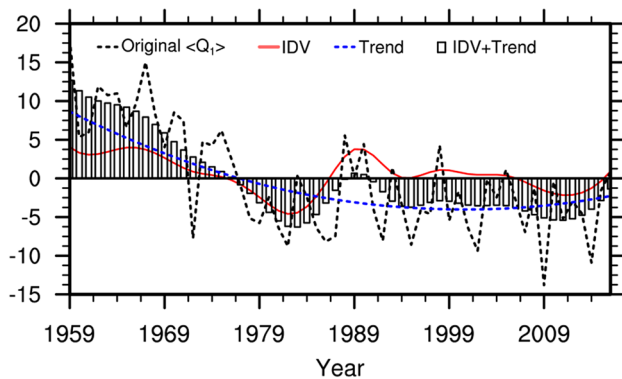


**Fig. 4** Original  $\langle Q_1 \rangle$  anomalies (black dashed curve; units:  $\text{W/m}^2$ ), EEMD-decomposed IDV (red curve), long-term trend component (dashed black curve) and the IDV plus trend (bar) for original  $\langle Q_1 \rangle$  during 1959–2016

between 1958 and 1982, reaching a minimum around 1982, followed by a gradual increase to a maximum in 1988. Since 1988, annual  $\langle Q_1 \rangle$  fluctuated around a certain range with a high peak in 1998, having a minimum value at approximately 2010. After 2010, the 11-year running mean of annual  $\langle Q_1 \rangle$  trended slightly upward. From 1958 to 2017,  $\langle Q_1 \rangle$  experienced obvious inter-decadal variability with distinct upward and downward phases. By applying the EEMD method to decompose the time series of  $\langle Q_1 \rangle$  anomalies over the TP, IDV was extracted to further examine the inter-decadal variation of  $\langle Q_1 \rangle$ . As shown in Fig. 4, IDV fully reflects the overall variability of  $\langle Q_1 \rangle$  at the inter-decadal timescale from 1959 to 2016. When IDV was in a downward phase during 1959–1982, it contributed to an accelerated weakening trend. After 1982, an upward swing in IDV was recorded, which balanced or reduced the decline during 1982–1999. However, these changes caused a slight upward trend after 1999. In a sense, IDV could enhance or suppress long-term trends due to the

comparable magnitude of IDV and long-term trend at the inter-decadal timescale.

### 3.2 IDV of $\langle Q_1 \rangle$ over the TP under the influence of IOSST and PDO

Since the decadal component is mainly induced by oceanic modes (Huang et al. 2016; Gan et al. 2019; Luo et al. 2019), we extracted the IDV of major oceanic modes to explore the influences of oceanic modes on the  $\langle Q_1 \rangle$  over the TP at the inter-decadal timescale. Correlations between IDV of annual  $\langle Q_1 \rangle$  and IDVs of each IOSST, PDO, ENSO, and Atlantic Multidecadal Oscillation (AMO) oceanic indices from 1959 to 2016 are shown in Fig. 5. IOSST (Fig. 5a) was negatively correlated with  $\langle Q_1 \rangle$  over most parts of the TP and the positive correlation was obvious in the western and southeastern TP. This result indicates that IOSST weakened  $\langle Q_1 \rangle$  over most parts of the TP and enhanced  $\langle Q_1 \rangle$  in the west and east of the Himalayas. Since PDO had an effect on IOSST at the inter-decadal timescale (Dong et al. 2016; Krishnamurthy and Krishnamurthy 2016), the spatial distribution of correlation between PDO and  $\langle Q_1 \rangle$  (Fig. 5b) was similar to that between IOSST and  $\langle Q_1 \rangle$  (Fig. 5a). ENSO (Fig. 5c) was also negatively correlated with  $\langle Q_1 \rangle$  over most parts of the TP. Nevertheless, the correlation between ENSO and  $\langle Q_1 \rangle$  was weaker than IOSST and PDO. AMO was negatively correlated with  $\langle Q_1 \rangle$  in the central and northeastern TP (Fig. 5d), and the positive correlation was obvious along the Himalayas. Comparison of results (Fig. 5a–d) suggest that IOSST, PDO, ENSO and AMO had close relationship with  $\langle Q_1 \rangle$  at the inter-decadal timescale, and relatively uniform weakening effects on  $\langle Q_1 \rangle$  in most parts of the TP, especially IOSST and PDO.

According to our results, conditional composite analysis based on IOSST-PDO's IDV phase relationship was conducted to identify the combined effect of IOSST and PDO over the TP at the inter-decadal timescale.  $\langle Q_1 \rangle$  composites associated with positive and negative IOSST phases during different PDO phases from 1959 to 2016 are illustrated in Fig. 6. Results indicate that anomalous  $\langle Q_1 \rangle$  was more significant under in-phase combinations (i.e., +IOSST/+PDO phase and -IOSST/-PDO phase) of IOSST and PDO (Fig. 6a, d) compared to the out-of-phase combinations (Fig. 6b, c; i.e., +IOSST/-PDO phase and -IOSST/+PDO phase).  $\langle Q_1 \rangle$  anomalies associated with positive IOSST phase during a positive PDO phase presented negative  $\langle Q_1 \rangle$  anomalies over the central and northeastern TP and positive  $\langle Q_1 \rangle$  anomalies over the western and southeastern parts of the Himalayas. In contrast,  $\langle Q_1 \rangle$  anomalies associated with the negative IOSST phase demonstrated an opposite structure during a negative PDO phase. Therefore, the combined effect of IOSST and PDO under in-phase conditions led to an obvious net loss (gain) of heat over the central and northeastern TP, while the



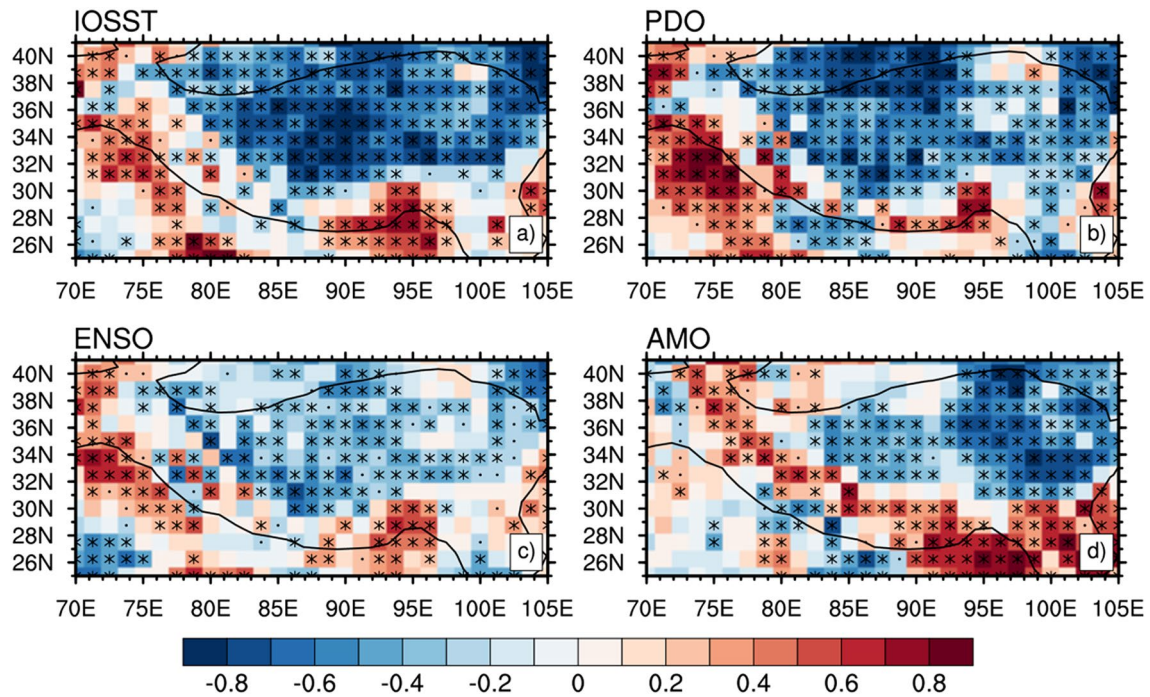


**Fig. 5** Correlation coefficients between IDV of annual  $\langle Q_1 \rangle$  and IDVs of oceanic indices: **a** IOSST with  $\langle Q_1 \rangle$ , **b** PDO with  $\langle Q_1 \rangle$ , **c** ENSO with  $\langle Q_1 \rangle$ , and **d** AMO with  $\langle Q_1 \rangle$ . The asterisk and black dot indi-

cates the 95% and 90% confidence level, respectively. Black contour indicates the elevation of 1800 m, as in Wu et al. (2015)

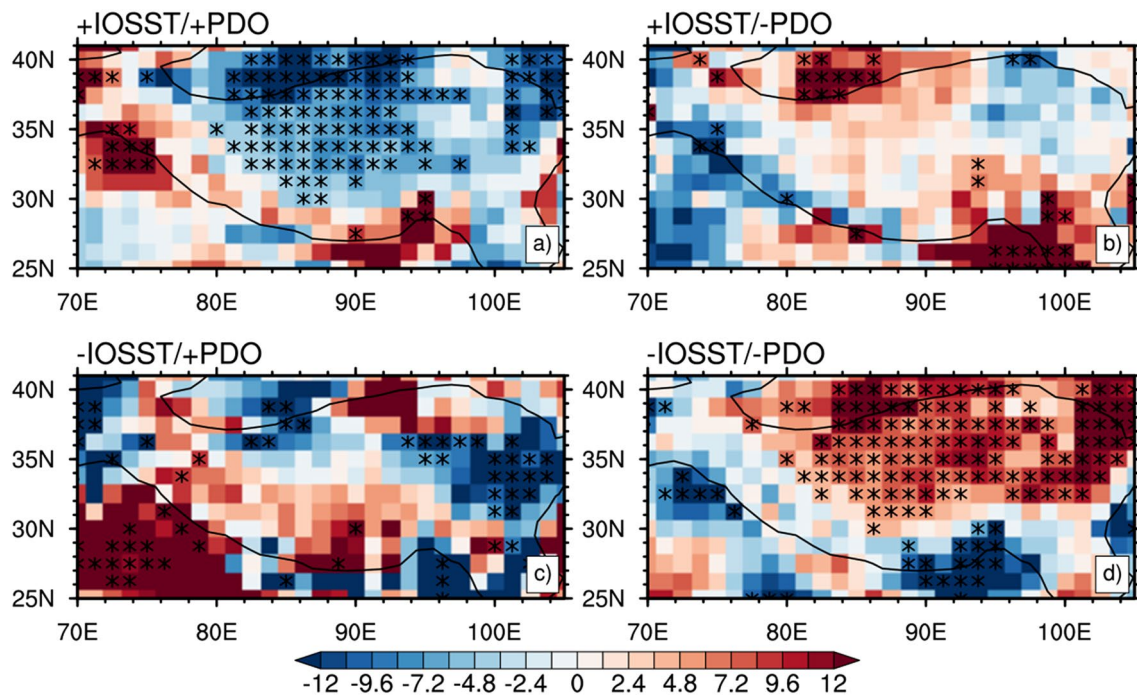


**Fig. 6** Conditional composite detrended annual  $\langle Q_1 \rangle$  anomalies (units:  $W/m^2$ ) over the TP for **a** +IOSST/+PDO, **b** +IOSST/-PDO, **c** -IOSST/+PDO, and **d** -IOSST/-PDO years. The asterisk indicates

the 90% confidence level. Black contour indicates the elevation of 1800 m, as in Wu et al. (2015)

out-of-phase combinations of IOSST and PDO composites did not exert a strong influence on heat budget over the TP.

To further understand how combinations of IOSST and PDO affect  $\langle Q_1 \rangle$  over the TP and to identify the physical processes involved, we examined annual geopotential height and wind fields. Composite analysis of the in-phase combination effects of IOSST and PDO on geopotential height and wind vector anomalies at 200 hPa are shown in Fig. 7. Two

low pressure systems in the northern Pacific and TP were identified when the positive IOSST was combined with the positive PDO (Fig. 7a). Cyclonic circulations transport cold air from the North Pacific and high latitudes toward the TP, carrying heat away causing net heat loss over the TP. On the contrary, low pressure systems changed to high pressure systems in the case of -IOSST/-PDO, and airflows brought warm air from the Indian Ocean, resulting in a net heat gain over the TP (Fig. 7b). Hence, in-phase combinations of the IOSST and PDO contribute to the heat budget over the TP at the inter-decadal timescale.

### 3.3 CMIP6 simulation of $\langle Q_1 \rangle$ over the TP

Based on extensive analysis of inter-decadal variability of  $\langle Q_1 \rangle$  over the TP, we intend to examine whether global climate models can better simulate the change of  $\langle Q_1 \rangle$  over the TP, thereby guiding future climate prediction over the TP. Although performances of global climate models available in the fifth phase of the Coupled Model Intercomparison Project (CMIP5) have already been evaluated over the TP (Su et al. 2013; You et al. 2016), CMIP6, the latest phase of the CMIP, needs to be validated for terms of  $\langle Q_1 \rangle$ . Therefore, in order to comprehensively reveal  $\langle Q_1 \rangle$  changes over the TP, we utilized historical simulations and future projections of 13 models in the CMIP6.

EEMD was used to decompose  $\langle Q_1 \rangle$  simulated by 13 CMIP6 models into IAV, IDV and R components, respectively, and to compare correlation coefficients between each historical component in different CMIP6 models with the corresponding component in JRA-55 reanalysis (Fig. 8). Results indicate that only two out of the 13 models for IAV have significant relationships, passing the 99% confidence level, and only CESM2 (0.36) has a positive correlation. Four out of the 13 models for IDV and 10 out of the 13 models for the R component which have significant relationships,

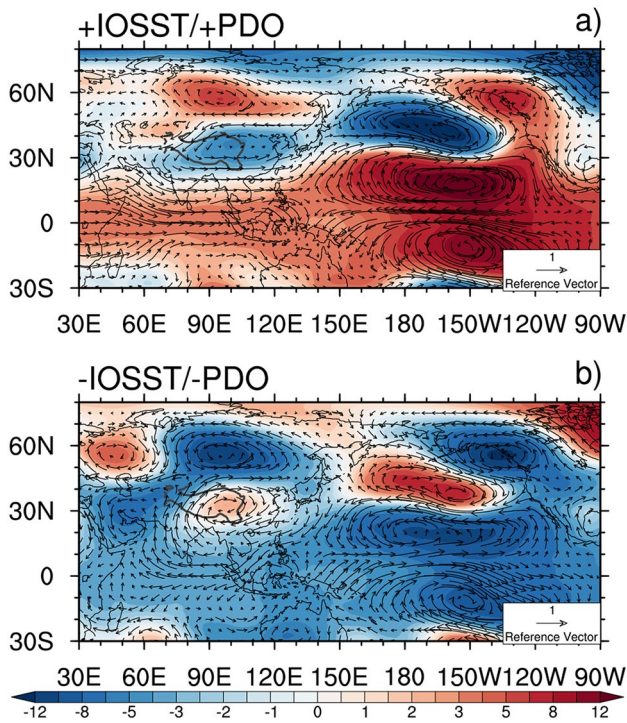
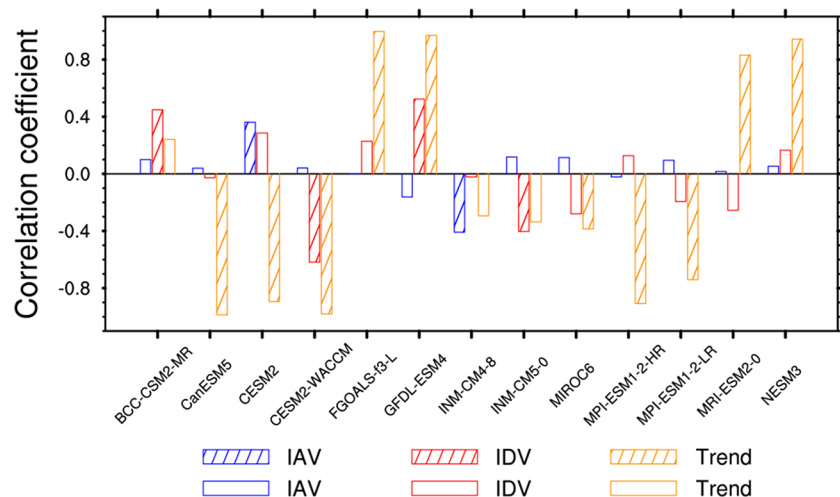


**Fig. 7** Conditional composite of detrended 200 hPa annual geopotential height (shading, units: gpm) and wind vector (vector, units: m/s) anomalies during 1959–2016 for **a** +IOSST/+PDO and **b** -IOSST/-PDO years

**Fig. 8** Correlation coefficients between CMIP6-simulated and JRA-55 IAV, IDV and R components of  $\langle Q_1 \rangle$ . Hatched bars indicate the correlation coefficients passing the 99% confidence level



passing the 99% confidence level. From the four correlated models of IDV, BCC-CSM2-MR (0.45) and GFDL-ESM4 (0.52) have positive correlations. From the 10 correlated models of trend component, FGOALS-f3-L (0.99), GFDL-ESM4 (0.97), MRI-ESM2-0 (0.83) and NESM3 (0.94) contain significant positive correlations. The statistical relationships between the 13 CMIP6 models and JRA-55 reanalysis indicate that CMIP6 historical simulations can't effectively simulate IAVs, but the simulations of IDV and trend components were relatively better.

The ensemble mean of historical simulation (Historical-EM) IDV by two correlated CMIP6 models is consistent with IDV of JRA-55 reanalysis during 1959–2013, having a significant correlation coefficient of 0.76 ( $p < 0.01$ ). This result was higher than both BCC-CSM2-MR and GFDL-ESM4 models and also better at reproducing the temporal evolutions of the IDV (Fig. 9). The phase changes of the Historical-EM IDV are nearly consistent with that of JRA-55 reanalysis (especially during 1971–1994). IDV of Historical-EM significantly declined from 1971, recording a minimum value in 1980, accompanied by the synchronous phase shift of the JRA-55 reanalysis. IDVs of the Historical-EM and JRA-55 reanalysis peaked in 1980 and decreased until 1991.

Subsequently, to understand how IDV will change under different scenarios, we examined future  $\langle Q_1 \rangle$  changes using 13 CMIP6 model projections. This was undertaken by initially adopting the continuous power spectrum to analyse the ensemble mean of all 13 CMIP6 models from future projections under SSP245 (SSP245-EM) and SSP585 (SSP585-EM) scenarios. This enabled us to analyze whether the dominant periodicity of  $\langle Q_1 \rangle$  over the TP is at the inter-decadal timescale. As presented in Fig. 10a, two obvious peaks were identified over inter-annual and inter-decadal timescales. In particular, the largest peak appeared at the inter-decadal timescale and it almost passed the significance test. This indicates that annual SSP245-EM  $\langle Q_1 \rangle$  has an obvious 15-year cycle. Meanwhile, the SSP585-EM  $\langle Q_1 \rangle$  appeared as distinct inter-decadal variability with a significant 30-year cycle (Fig. 11a).

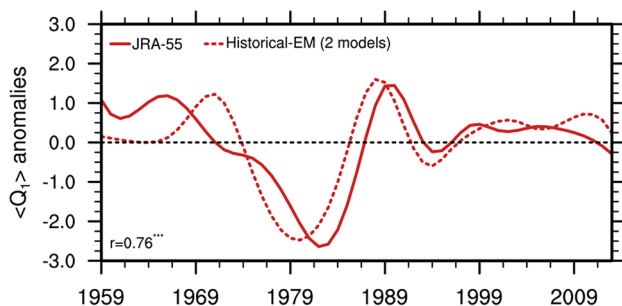


**Fig. 9** Time series of the standardized JRA-55 IDV (thick solid curve) and Historical-EM IDV (thick dashed curve) of two correlated CMIP6 models for  $\langle Q_1 \rangle$  during 1959–2013. Symbol \*\*\* indicates the statistical significance is above the 99% confidence level

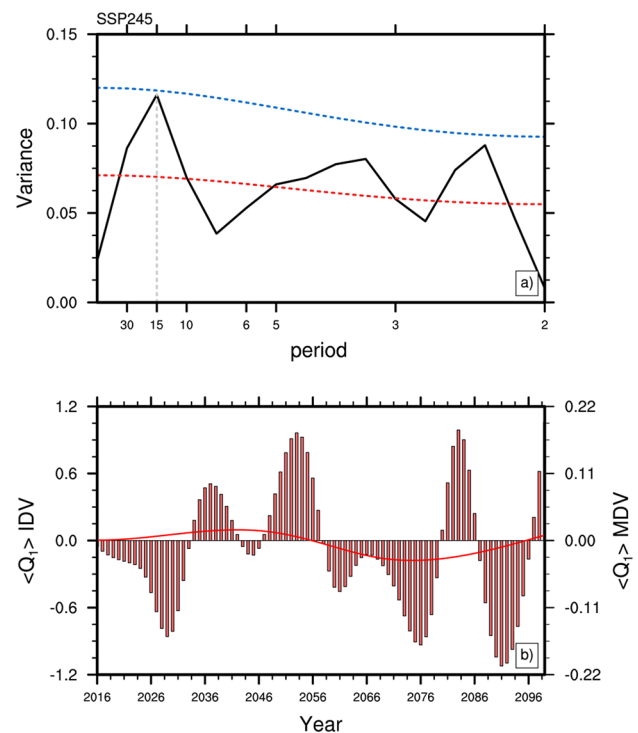


**Fig. 10** a Power spectrum of annual SSP245-EM  $\langle Q_1 \rangle$  anomalies over the TP during 2015–2100. The blue and red dashed lines show the 90% confidence level and the reference red noise spectrum, respectively. b The SSP245-EM IDV (bars) and MDV (red curve) of annual  $\langle Q_1 \rangle$  anomalies during 2016–2099

As a distinct inter-decadal periodicity of  $\langle Q_1 \rangle$  was identified in the future, the EEMD method was also applied to extract IDV of future  $\langle Q_1 \rangle$ .

Since future projections of CMIP6 involve a future period of 86 years (from 2015 to 2100), which takes an obvious change of amplitude on the multi-decadal variability (MDV) component. The MDV of  $\langle Q_1 \rangle$  can be decomposed using the EEMD method. We then compared IDV and MDV of SSP245-EM  $\langle Q_1 \rangle$  (Fig. 10b) and SSP585-EM  $\langle Q_1 \rangle$  (Fig. 11b). Relative to IDV of SSP245-EM  $\langle Q_1 \rangle$ , the amplitude of IDV will decrease and the cycle of IDV will contract under high radiative forcing (i.e., SSP585). On the contrary, the amplitude of MDV increased under the SSP585 scenario and the MDV phase was opposite to that under the SSP245 scenario. Hence, the inter-decadal variation was the dominant periodicities of  $\langle Q_1 \rangle$  and high radiative forcing will have different effects on the cycle and amplitude of  $\langle Q_1 \rangle$  at the inter-decadal and multi-decadal timescales in the future.



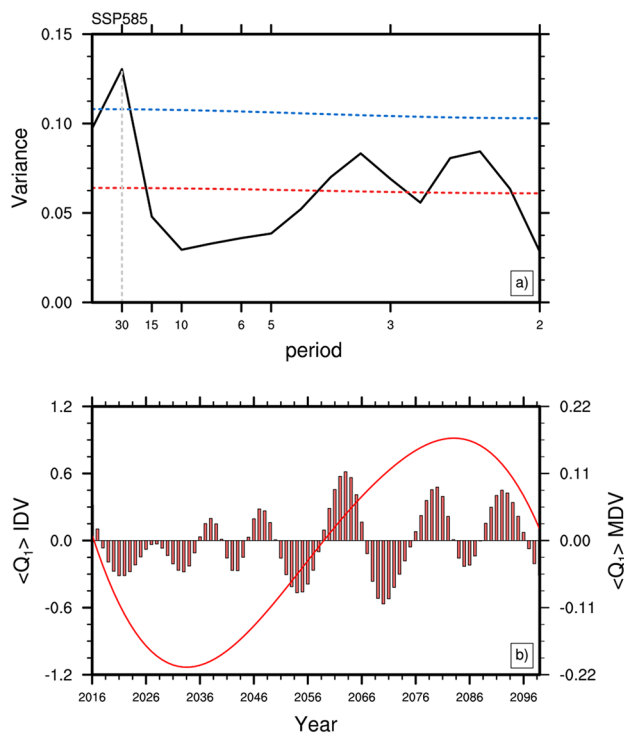


Fig. 11 Same as Fig. 10, except for SSP585-EM  $\langle Q_1 \rangle$

## 4 Conclusions and discussion

In this study, we revealed that  $\langle Q_1 \rangle$  over the TP has distinct inter-decadal variation in its temporal variation. Such variation is closely related to the effects of oceanic modes, where IOSST and PDO have a key role in the variation of  $\langle Q_1 \rangle$  at the inter-decadal timescale. According to composite analysis, spatiotemporal variations of  $\langle Q_1 \rangle$  are closely related to the in-phase combinations of IOSST and PDO. When the IOSST and PDO are both in positive (negative) phase, low pressure (high pressure) system occurs over the TP and cyclonic (anticyclone) circulation brings cold (warm) air from the North Pacific (Indian Ocean), leading to an obvious net loss (gain) of heat over the central and northeastern TP. However, the heat budget over the TP is moderately affected by the out-of-phase combinations of IOSST and PDO. The inter-decadal variation will be the dominant periodicities of  $\langle Q_1 \rangle$  in future projections of CMIP6, with the intensification of the emission scenario, high radiative forcing will reduce the amplitude and shorten the cycle of IDV but enhance the amplitude of MDV which will lead to the prolongation of the dominant periodicity of the  $\langle Q_1 \rangle$  in the future.

Duan and Wu (2009) explored decadal thermal forcing over the TP, indicating its close relation to the variation of the subtropical westerly jet (Liu et al. 2012) and its enhancement by the positive SST anomaly tripole pattern over the North Atlantic (Cui et al. 2015). Recent climate changes

have weakened surface sensible heat and enhanced atmospheric radiative cooling over the TP (Duan et al. 2013; Wu et al. 2015; Zhao et al. 2018), which in turn weakened the thermal forcing of the TP. Besides, the heat budget over the TP is also affected by other external factors (e.g., cloud cover, snow/ice-albedo feedback) (Liu and Chen 2000). Therefore, the regional variation of weather and climate over the TP is usually caused by different factors in a simultaneous manner (due to the climate system being nonlinear, open and a dissipative system) (Wu et al. 2017). Further investigations will be needed to elucidate the mechanisms of the various climate system factors or physical processes synergistic influence and determine their underlying interactions over the TP.

**Acknowledgements** This work was jointly supported by the National Science Foundation of China (42041004, 41521004), the Strategic Priority Research Program of Chinese Academy of Sciences (Grant No. XDA2006010301), the China 111 project (No. B13045) and the Central universities (Izujbky-2019-kb30). The HadISST (version 1.1) is available at <https://www.metoffice.gov.uk/hadobs/hadisst/>. The PDO index is available at [http://jisao.washington.edu/data\\_sets/pdo/](http://jisao.washington.edu/data_sets/pdo/). And the CMIP6 outputs are available at <https://esgf-node.llnl.gov/projects/cmip6/>. The authors wish to thank three reviewers for their constructive suggestions.

## References

- Birk K, Lupo AR, Guinan PE, Barbieri CE (2010) The interannual variability of midwestern temperatures and precipitation as related to the ENSO and PDO. *Atmosfera* 23:95–128
- Cao J (2019) NUIST NESMv3 model output prepared for CMIP6 CMIP Version 20190728 Earth System Grid Federation. <https://doi.org/10.22033/ESGF/CMIP6.8790>
- Chen G, Iwasaki T, Qin H, Sha W (2014) Evaluation of the warm-season diurnal variability over East Asia in recent reanalyses JRA-55, ERA-interim, NCEP CFSR, and NASA MERRA. *J Clim* 27:5517–5537. <https://doi.org/10.1175/jcli-d-14-00005.1>
- Cui Y, Duan A, Liu Y et al (2015) Interannual variability of the spring atmospheric heat source over the Tibetan Plateau forced by the North Atlantic SSTA. *Clim Dyn* 45:1617–1634. <https://doi.org/10.1007/s00382-014-2417-9>
- Danabasoglu G (2019) NCAR CESM2-WACCM model output prepared for CMIP6 CMIP Version 20191105 Earth System Grid Federation. <https://doi.org/10.22033/ESGF/CMIP6.10101>
- Dong L, Zhou T, Dai A et al (2016) The footprint of the inter-decadal Pacific oscillation in Indian Ocean sea surface temperatures. *Sci Rep* 6:21251. <https://doi.org/10.1038/srep21251>
- Duan A, Wu G (2008) Weakening trend in the atmospheric heat source over the Tibetan Plateau during recent decades. Part I: observations. *J Clim* 21:3149–3164. <https://doi.org/10.1175/2007JCLI1912.1>
- Duan A, Wu G (2009) Weakening trend in the atmospheric heat source over the Tibetan Plateau during recent decades. Part II: connection with climate warming. *J Clim* 22:4197–4212. <https://doi.org/10.1175/2009JCLI2699.1>
- Duan A, Wu G, Liu Y, Ma Y, Zhao P (2012) Weather and climate effects of the Tibetan Plateau. *Adv Atmos Sci* 29:978–992. <https://doi.org/10.1007/s00376-012-1220-y>

- Duan A, Wang M, Lei Y, Cui Y (2013) Trends in summer rainfall over china associated with the tibetan plateau sensible heat source during 1980–2008. *J Clim* 26:261–275. <https://doi.org/10.1175/JCLI-D-11-00669.1>
- Gan Z, Guan X, Kong X, Guo R, Huang H, Huang W, Xu Y (2019) The key role of Atlantic Multidecadal Oscillation in minimum temperature over North America during global warming slowdown. *Earth Space Sci* 6:387–397. <https://doi.org/10.1029/2018EA000443>
- He B, Liu Y, Wu G, Wang Z, Bao Q (2019) The role of air–sea interactions in regulating the thermal effect of the Tibetan–Iranian Plateau on the Asian summer monsoon. *Clim Dyn* 52:4227–4245. <https://doi.org/10.1007/s00382-018-4377-y>
- Huang NE, Shen Z, Long SR, Wu MC, Shih HH, Zheng Q et al (1998) The empirical mode decomposition and the Hilbert spectrum for nonlinear and non-stationary time series analysis. *Proc R Soc London Ser A Math Phys* 454:903–995. <https://doi.org/10.1098/rspa.1998.0193>
- Huang J, Xie Y, Guan X, Li D, Ji F (2016) The dynamics of the warming hiatus over the Northern Hemisphere. *Clim Dyn* 48:429–446. <https://doi.org/10.1007/s00382-016-3085-8>
- Ji F, Wu Z, Huang J, Chassignet EP (2014) Evolution of land surface air temperature trend. *Nat Clim Chang* 4:462–466. <https://doi.org/10.1038/nclimate2223>
- Jin R, Qi L, He J (2016) Effect of oceans to spring surface sensible heat flux over Tibetan Plateau and its influence to East China precipitation. *Acta Oceanol Sin* 38:83–95. <https://doi.org/10.3969/j.issn.0253-4193.2016.05.008> (in Chinese)
- John J, Blanton C, McHugh C, Nikonov S et al (2018) NOAA-GFDL GFDL-ESM4 model output prepared for CMIP6 CMIP Version 20180701 Earth System Grid Federation. <https://doi.org/10.22033/ESGF/CMIP6.8706>
- Kim JW, Yeh SW, Chang EC (2014) Combined effect of El Niño–Southern Oscillation and Pacific Decadal Oscillation on the East Asian winter monsoon. *Clim Dyn* 42:957–971. <https://doi.org/10.1007/s00382-013-1730-z>
- Kobayashi S, Ota Y, Harada Y, Ebata A, Morioka M, Onoda H et al (2015) The JRA-55 reanalysis: general specifications and basic characteristics. *J Meteorol Soc Jpn Ser II* 93:5–48. <https://doi.org/10.2151/jmsj.2015-001>
- Krishnamurthy L, Krishnamurthy V (2016) Decadal and interannual variability of the Indian Ocean SST. *Clim Dyn* 46(1–2):57–70. <https://doi.org/10.1007/s00382-015-2568-3>
- Li X, Wang L, Guo X, Chen D (2017) Does summer precipitation trend over and around the Tibetan Plateau depend on elevation? *Int J Climatol*. <https://doi.org/10.1002/joc.4978>
- Liu X, Chen B (2000) Climatic warming in the Tibetan Plateau during recent decades. *Int J Climatol* 20:1729–1742. [https://doi.org/10.1002/1097-0088\(20001130\)20:14%3c1729::AID-JOC556%3e3.0.CO;2-Y](https://doi.org/10.1002/1097-0088(20001130)20:14%3c1729::AID-JOC556%3e3.0.CO;2-Y)
- Liu G, Zhao P, Wu R, Chen J (2012) Potential flaws of interdecadal changes over eastern China around the early 1990s in the National Centers for Environmental Prediction–National Center for atmospheric research reanalyses. *J Geophys Res Atmos* 117:D02111. <https://doi.org/10.1029/2011JD016327>
- Luo W, Guan X, Xie Y, Liu J, Zhou Y, Zhang B (2019) The key role of decadal modulated oscillation in recent cold phase. *Int J Climatol*. <https://doi.org/10.1002/joc.6186>
- Ma J, Guan X, Guo R, Gan Z, Xie Y (2017) Mechanism of non-appearance of hiatus in Tibetan Plateau. *Sci Rep* 7:4421. <https://doi.org/10.1038/s41598-017-04615-7>
- Mantua NJ, Hare SR, Zhang Y, Wallace JM, Francis RC (1997) A Pacific Interdecadal Climate Oscillation with impacts on Salmon Production. *Bull Amer Meteorol Soc* 78:1069–1079. [https://doi.org/10.1175/1520-0477\(1997\)078%3c1069:APICOW%3e2.0.CO;2](https://doi.org/10.1175/1520-0477(1997)078%3c1069:APICOW%3e2.0.CO;2)
- Meehl GA, Moss R, Taylor KE, Eyring V, Stouffer RJ, Bony S et al (2014) Climate model intercomparisons: preparing for the next phase. *EOS Trans Am Geophys Union* 95:77–78. <https://doi.org/10.1002/2014eo090001>
- O'Neill BC, Kriegler E, Riahi K, Ebi KL, Hallegatte S, Carter TR et al (2014) A new scenario framework for climate change research: the concept of shared socioeconomic pathways. *Clim Change* 122:387–400. <https://doi.org/10.1007/s10584-013-0905-2>
- O'Neill BC, Tebaldi C, van Vuuren DP, Eyring V, Friedlingstein P, Hurtt G (2016) The scenario model intercomparison project (Scenario MIP) for CMIP6. *Geosci Model Dev* 9:3461–3482. <https://doi.org/10.5194/gmd-9-3461-2016>
- Parker DE, Folland CK, Jackson M (1995) Marine surface temperature: observed variations and data requirements. *Clim Change* 31:559–600. <https://doi.org/10.1007/bf01095162>
- Qian C, Wu Z, Fu C, Wang D (2011) On changing El Niño: a view from time-varying annual cycle, interannual variability and mean state. *J Clim* 24:6486–6500. <https://doi.org/10.1175/jcli-d-10-05012.1>
- Rayner NA, Parker DE, Horton EB, Folland CK, Alexander LV, Rowell DP, Kent EC, Kaplan A (2003) Global analyses of sea surface temperature, sea ice, and night marine air temperature since the late nineteenth century. *J Geophys Res* 108:4407. <https://doi.org/10.1029/2002JD002670>
- Reynolds RW, Rayner NA, Smith TM, Stokes DC, Wang W (2002) An improved in situ and satellite SST analysis for climate. *J Clim* 15:1609–1625. [https://doi.org/10.1175/1520-0442\(2002\)015%3c1609:AIISAS%3e2.0.CO;2](https://doi.org/10.1175/1520-0442(2002)015%3c1609:AIISAS%3e2.0.CO;2)
- Schupfner M, Wieners K, Wachsmann F, Steger C et al (2019) DKRZ MPI-ESM1.2-HR model output prepared for CMIP6 CMIP Version 20190710 Earth System Grid Federation. <https://doi.org/10.22033/ESGF/CMIP6.4403>
- Shiogama H, Abe M, Tatebe H (2019) MIROC MIROC6 model output prepared for CMIP6 CMIP Version 20191114 Earth System Grid Federation. <https://doi.org/10.22033/ESGF/CMIP6.5746>
- Su F, Duan X, Chen D, Hao Z, Cuo L (2013) Evaluation of the global climate models in the CMIP5 over the Tibetan Plateau. *J Clim* 26:3187–3208. <https://doi.org/10.1175/jcli-d-12-00321.1>
- Swart N, Cole J, Kharin V, Lazare M et al (2019) CCCma CanESM5 model output prepared for CMIP6 CMIP Version 20190429 Earth System Grid Federation. <https://doi.org/10.22033/ESGF/CMIP6.3685>
- van Vuuren DP, Kriegler E, O'Neill BC, Ebi KL, Riahi K, Carter TR et al (2014) A new scenario framework for climate change research: scenario matrix architecture. *Clim Change* 122:373–386. <https://doi.org/10.1007/s10584-013-0906-1>
- Volodin E, Mortikov E, Gritsun A, Lykossov V et al (2019a) INM INM-CM4–8 model output prepared for CMIP-6 CMIP Version 20190605 Earth System Grid Federation. <https://doi.org/10.22033/ESGF/CMIP6.12327>
- Volodin E, Mortikov E, Gritsun A, Lykossov V et al (2019b) INM INM-CM5-0 model output prepared for CMIP-6 CMIP Version 20190724 Earth System Grid Federation. <https://doi.org/10.22033/ESGF/CMIP6.12338>
- Wang Z, Yang S, Lau NC, Duan A (2018) Teleconnection between summer NAO and East China rainfall variations: a bridge effect of the Tibetan Plateau. *J Clim* 31:6433–6444. <https://doi.org/10.1175/JCLI-D-17-0413.1>
- Wang M, Wang J, Duan A, Yang J, Liu Y (2019) Quasi-biweekly impact of the atmospheric heat source over the Tibetan Plateau on summer rainfall in Eastern China. *Clim Dyn* 53:4489–4504. <https://doi.org/10.1007/s00382-019-04798-x>
- Wei M, Qiao F, Guo Y, Deng J, Song Z, Shu Q, Yang X (2019) Quantifying the importance of interannual, interdecadal and multi-decadal climate natural variabilities in the modulation of global warming rates. *Clim Dyn* 53:6715–6727. <https://doi.org/10.1007/s00382-019-04955-2>

- Wieners K, Giorgetta M, Jungclaus J, Reick C et al (2019) MPI-M MPI-ESM1.2-LR model output prepared for CMIP6 CMIP Version 20190710 Earth System Grid Federation. <https://doi.org/10.22033/ESGF/CMIP6.6705>
- Wu G, Zhang Y (1998) Tibetan Plateau forcing and the timing of the monsoon onset over South Asian and the South China Sea. *Mon Weather Rev* 126:913–927. [https://doi.org/10.1175/1520-0493\(1998\)126<0913>2.0.CO;2](https://doi.org/10.1175/1520-0493(1998)126<0913>2.0.CO;2)
- Wu G, Liu Y, Zhang Q, Duan A, Wang T, Wan R et al (2007) The influence of mechanical and thermal forcing by the Tibetan Plateau on Asian climate. *J Hydrometeorol* 8:770–789. <https://doi.org/10.1175/JHM609.1>
- Wu Z, Huang NE, Wallace JM, Smoliak BV, Chen X (2011) On the time-varying trend in global-mean surface temperature. *Clim Dyn* 37:759–773. <https://doi.org/10.1007/s00382-011-1128-8>
- Wu G, Liu Y, He B, Bao Q, Duan A, Jin F (2012) Thermal controls on the Asian summer monsoon. *Sci Rep* 2:404. <https://doi.org/10.1038/srep00404>
- Wu G, Duan A, Liu Y, Mao J, Ren R, Bao Q et al (2015) Tibetan plateau climate dynamics: recent research progress and outlook. *Natl Sci Rev* 2:100–116. <https://doi.org/10.1093/nsr/nwu045>
- Wu G, He B, Duan A, Liu Y, Yu W (2017) Formation and variation of the atmospheric heat source over the Tibetan Plateau and its climate effects. *Adv Atmos Sci* 34:1169–1184. <https://doi.org/10.1007/s00376-017-7014-5>
- Wu Y, Yang S, Hu X, Wei W (2020) Process-based attribution of long-term surface warming over the Tibetan Plateau. *Int J Climate*. <https://doi.org/10.1002/joc.6589>
- Xie T, Li J, Chen K, Zhang Y, Sun C (2021) Origin of Indian Ocean multidecadal climate variability: role of the North Atlantic Oscillation. *Clim Dyn*. <https://doi.org/10.1007/s00382-021-05643-w>
- Xin X, Wu T, Shi X, Zhang F et al (2019) BCC BCC-CSM2MR model output prepared for CMIP6 CMIP Version 20190315 Earth System Grid Federation. <https://doi.org/10.22033/ESGF/CMIP6.3030>
- Yanai M, Tomita T (1998) Seasonal and interannual variability of atmospheric heat sources and moisture sinks as determined from NCEP–NCAR reanalysis. *J Clim* 11:463–482. [https://doi.org/10.1175/1520-0442\(1998\)011<0463:SAIVOA>2.0.CO;2](https://doi.org/10.1175/1520-0442(1998)011<0463:SAIVOA>2.0.CO;2)
- Yanai M, Esbensen S, Chu JH (1973) Determination of bulk properties of tropical cloud clusters from large-scale heat and moisture budgets. *J Atmos Sci* 30:611–627. [https://doi.org/10.1175/1520-0469\(1973\)030<0611:DOBPOT>3e2.0.CO;2](https://doi.org/10.1175/1520-0469(1973)030<0611:DOBPOT>3e2.0.CO;2)
- Yang K, Wu H, Qin J, Lin C, Tang W, Chen Y (2014) Recent climate changes over the Tibetan Plateau and their impacts on energy and water cycle: a review. *Glob Planet Change* 112:79–91. <https://doi.org/10.1016/j.gloplacha.2013.12.001>
- You Q, Min J, Kang S (2016) Rapid warming in the Tibetan Plateau from observations and CMIP5 models in recent decades. *Int J Climatol* 36:2660–2670. <https://doi.org/10.1002/joc.4520>
- Yu Y (2019) CAS FGOALS-f3-L model output prepared for CMIP6 CMIP Version 20191013 Earth System Grid Federation. <https://doi.org/10.22033/ESGF/CMIP6.3468>
- Yukimoto S, Koshiro T, Kawai H, Oshima N et al (2019) MRI MRI-ESM2.0 model output prepared for CMIP6 CMIP Version 20191108 Earth System Grid Federation. <https://doi.org/10.22033/ESGF/CMIP6.6929>
- Zhang Y, Wallace JM, Battisti DS (1997) ENSO-like interdecadal variability: 1900–93. *J Clim* 10:1004–1020. [https://doi.org/10.1175/1520-0442\(1997\)010<1004:ELIV>3e2.0.CO;2](https://doi.org/10.1175/1520-0442(1997)010<1004:ELIV>3e2.0.CO;2)
- Zhao Y, Duan A, Wu G (2018) Interannual variability of late-spring circulation and diabatic heating over the Tibetan Plateau associated with Indian Ocean forcing. *Adv Atmos Sci* 35:927–941. <https://doi.org/10.1007/s00376-018-7217-4>
- Zhou X, Zhao P, Chen J, Chen L, Li W (2009) Impacts of thermodynamic processes over the Tibetan Plateau on the Northern Hemispheric climate. *Sci China* 52:1679–1693. <https://doi.org/10.1007/s11430-009-0194-9>
- Zhu L, Huang G, Fan G, Qü X, Wang Z, Hua W (2018) Elevation-dependent sensible heat flux trend over the Tibetan Plateau and its possible causes. *Clim Dyn* 52(7–8):3997–4009. <https://doi.org/10.1007/s00382-018-4360-7>

**Publisher's Note** Springer Nature remains neutral with regard to jurisdictional claims in published maps and institutional affiliations.